



OPEN An in silico evaluation of signal and separability properties of k-edge materials in spectral CT

Jayasai R. Rajagopal^{1,2}, Faraz Farhadi², Pooyan Sahbaee³, Elizabeth C. Jones²✉, Ehsan Samei¹ & William F. Pritchard²

Spectral CT can acquire signal at multiple x-ray energy levels. This enables material quantification by exploiting differences in x-ray attenuation across energy levels, particularly for k-edge materials. This simulation study quantified the signal and separability of current and potential clinical contrast agents across a range of materials and energies. A validated CT simulation platform was used to simulate a clinical photon-counting CT scanner with two energy thresholds. A cylindrical phantom containing common biological materials, clinical contrast agents, candidate contrast agents and nanoparticles, and investigational materials was imaged with varying upper energy thresholds (50–90 keV). At each energy level, images were assessed for noise, each material was assessed for contrast, and each material pair was evaluated for separability. Material contrasts reached peak value at the closest threshold higher than their respective k-edge. The energy threshold that produced the highest separability for each pair was characterized. Selection of energy threshold was dependent on the materials of interest. Threshold values at or just above a material's k-edge maximized material signal while separability was maximized by the threshold that best separated k-edge signals.

Since its invention in the 1970s, x-ray based computed tomography (CT) has been a premier imaging modality for diagnostic imaging. The number of CT scans^{1,2} has increased over time across the globe. CT plays an important role in diagnosis for a variety of areas including thoracic, abdominal, cardiac, neurological, musculoskeletal, oncologic, and emergency care. This role can be attributed to the many benefits of CT including high spatial resolution, volumetric imaging, tissue contrast, and short scan time³.

The mechanism that enables computed tomography is photon attenuation. Attenuation⁴ describes the loss of flux as a photon beam passes through any object. Attenuation is determined by the length of material that photons pass through, the composition of those materials, and the energy of the photon. CT exploits this behavior to discriminate between tissues with subtly different radiographic contrast, that is, differences in x-ray attenuation. To improve differentiation of different soft tissues, which have similar material compositions, contrast agents can be used to improve the attenuation of target tissues. The most commonly used contrast agent in clinical CT is iodine. The addition of a contrast agents enables a number of applications including organ and tissue characterization, angiography, perfusion studies, and tumor differentiation.

Conventional computed tomography relies on an integrated x-ray energy spectrum for material discrimination. Spectral CT^{5,6} represents an extension of conventional CT by acquiring spectral CT image data simultaneously or near simultaneously at multiple energy levels. Clinical systems primarily use dual-energy implementations⁷, which use a variety of techniques⁸ to acquire two energy levels at once. More recently, photon-counting CT (PCCT) has offered a new method to obtain spectral information using a different detection method than conventional CT, enabling acquisition of images at more than two energy levels^{9,10} and processing that information in a variety of post-processing options¹¹. Some post-processing options generate images that only contain specific portions of acquired signal, such as virtual non-contrast images^{12,13} and virtual monoenergetic images^{14,15}. Other methods enable domain transformation from signal intensity. Examples include rho-effective Z^{16,17}, photoelectric-Compton scatter¹⁸, and basis material decomposition¹⁹.

Material decomposition is a technique that uses signal acquired at multiple energies to quantify the location and amount of materials. Material specific characterization is possible as materials have different attenuations at different x-ray energy levels. This technique is particularly potent when taking advantage of the k-edge effect.

¹Carl E. Ravin Advanced Imaging Laboratories and Center for Virtual Imaging Trials, Department of Radiology, Duke University Medical Center, Durham, NC 27705, USA. ²Radiology and Imaging Sciences, National Institutes of Health Clinical Center, Bethesda, MD 20892, USA. ³Siemens Healthineers, Malvern, PA 19335, USA. ✉email: ejones@cc.nih.gov

The k-edge effect is caused by a discontinuous increase in signal at certain energy levels due to the photo-electric effect, the interaction of x-ray photons at or above the binding energy of an atoms k-shell electrons^{20–22}. Different materials have different k-edge levels, including iodine at 33.2 keV. Material decomposition applications can be further enhanced when considering multiple k-edge materials used in concert to target different anatomies or functions. Pre-clinical investigations have studied multi-phase multi-contrast applications²³ and using multiple contrast agents for different anatomical regions^{24,25}.

While iodine is the primary clinical contrast agent, there are many elements with k-edge energies in the range of diagnostic x-rays that are promising candidates for k-edge imaging²⁶. Both gadolinium^{27,28} and bismuth²⁹ have been investigated as contrast agents in CT. As an alternative to liquid contrast agents, studies have also focused on several nanoparticle agents^{30–32} and on drug eluting beads^{33,34} for therapeutic applications. The introduction of new contrast agents increases the capabilities of CT to include multi-contrast agent studies^{23,24,35} and functional imaging applications^{36,37}.

While earlier investigations of candidate materials have focused on identifying viable contrast agents and optimization of tube voltage for imaging an agent^{38,39}, there are some challenges to pursuing further experimental comparisons. Acquisition and synthesis of required material compounds can be difficult and requires specialized equipment or expertise. Further, inhomogeneities within solutions can complicate validation of the imaged ground truth. As an alternative, virtual imaging trials^{40–42} can address these challenges. Physics-based simulations can accurately reflect reality while reducing cost and complexity into the computational domain and providing a known ground truth.

One important consideration with potential new contrast agents is how those materials affect signal in spectral CT acquisitions. For clinical applications, the knowledge of acquisition parameters is important to maximize signal and to produce the best clinical outcomes. Further, as spectral CT becomes more integrated in the clinic, there is an increased opportunity for multi-contrast agent imaging. The relationship between pairs of k-edge materials and their signal responses under different energy separation conditions has been underreported. The goal of this work was to characterize the signal and separability properties of materials in relation to photon-counting CT energy thresholds and provide a framework for future development. This was done by applying an established spectral metrology to simulated data using a validated simulation platform, DukeSim⁴³. Materials used in this study included common biological elements, current contrast agents, and candidate k-edge materials. The dependence of contrast properties and material separability was characterized as a function of energy threshold.

Results

Virtual Phantom design

This study used a cylindrical computational (30 cm) phantom containing 16 inserts (Fig. 1). The background of the phantom was filled with water and inserts were filled with materials of interest at fixed concentrations. Materials were chosen to represent elements found in the body (calcium, iron), currently used contrast agents (iodine, barium), candidate contrast agents (gadolinium^{27,44}, bismuth²⁹, candidate nanoparticle materials (ytterbium^{45,46}, tantalum^{47,48}, tungsten⁴⁹, gold^{50,51}, platinum⁵², and lanthanides that did not fall into the other groups (samarium, europium, terbium, lutetium). Table 1 provides details of each material including their k-edge and reason for inclusion. Material concentrations were matched to iodine for contrast agents and nanomaterials. Calcium and iron concentrations were chosen to match the lowest concentration of inserts in commercial dual-energy phantoms.

For further evaluations, materials were grouped into three categories based on function and range of k-edge values: common biological materials and current clinical contrast agents (barium, calcium, gadolinium, iron, iodine), lanthanides (europium, gadolinium, lutetium, samarium, terbium), and candidate contrast agents and nanomaterials (bismuth, gold, platinum, tantalum, tungsten, ytterbium).

Image quality

Image quality metrics were evaluated to gain an understanding of the relationship between material signal and energy thresholds. Regions of interest (ROIs) were drawn in each insert and water background. Water background ROIs were used to calculate noise which represents the uncertainty associated with each signal condition. Contrast was evaluated as the difference between signal in each insert and background which represents the detected signal for each material at each energy threshold.

As the upper energy threshold was increased from 50 to 90 keV, the noise in the lower energy image fell from 16.0 to 11.8 HU while it increased in the high energy image from 13.0 to 33.6 HU (Fig. 2).

For the first group of materials (Fig. 3a), containing common biological materials and current clinical contrast agents, contrast in the lower energy image increased with energy threshold before peaking at 70 keV. For the higher energy image, contrast fell as the energy threshold was increased. Calcium, the material with the highest concentration in the dataset, had the highest contrast across all thresholds and images.

For the second group of materials (Fig. 3b), containing the lanthanides, contrast in the lower energy image increased steadily with energy threshold and began to plateau after 70 keV. In the higher energy image, contrast decreased as energy threshold increased for all materials except lutetium which instead peaked at 65 keV. Across all the lanthanides included in this dataset, lutetium had the lowest contrast in the low energy image for each threshold but had the highest contrast in the high energy image for every energy threshold greater than 60 keV.

For the third group of materials (Fig. 3c), containing high-Z candidate contrast agents and nanomaterials, contrast increased with energy threshold in the low energy image for tantalum, tungsten, and ytterbium. Bismuth, gold, platinum, and ytterbium reached a peak value at 70 keV after which the contrast decreased. For the high energy image, the contrast of tantalum, tungsten, and ytterbium reached peak values between 60 and

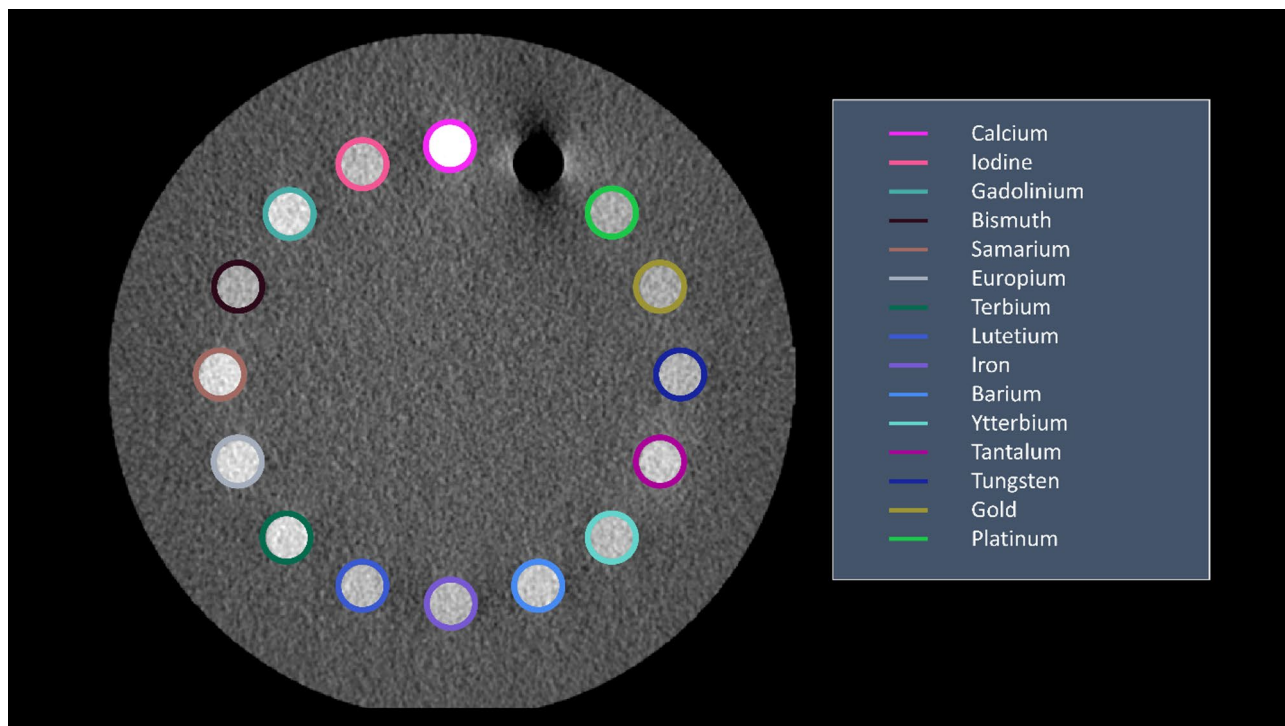


Fig. 1. Low energy threshold (20–50 keV) image of cylindrical computational phantom. The colored rings identify the different materials of interest. Background is water. Image presented with window width/window level of 300/40.

Element	k-edge (keV)	Concentration	Reason for inclusion
Calcium (Ca)	4	50 mg/mL	Commonly found in the body
Iron (Fe)	7	30 mg/mL	Commonly found in the body
Iodine (I)	33	4 mg/mL	Currently used contrast agent
Barium (Ba)	37	4 mg/mL	Currently used as a contrast agent
Samarium (Sm)	47	4 mg/mL	Investigational usage
Europium (Eu)	49	4 mg/mL	Investigational usage
Gadolinium (Gd)	50	4 mg/mL	Currently used contrast agent for MRI and candidate agent for CT
Terbium (Tb)	52	4 mg/mL	Investigational usage
Ytterbium (Yb)	61	4 mg/mL	Candidate nanoparticle agent
Lutetium (Lu)	63	4 mg/mL	Investigational usage
Tantalum (Ta)	67	4 mg/mL	Candidate nanoparticle agent
Tungsten (W)	70	4 mg/mL	Candidate nanoparticle agent
Platinum (Pt)	78	4 mg/mL	Candidate nanoparticle agent
Gold (Au)	81	4 mg/mL	Candidate nanoparticle agent
Bismuth (Bi)	91	4 mg/mL	Candidate contrast agent

Table 1. Elements used in this study, including their k-edges, the concentrations used, and the reason for inclusion.

70 keV before decreasing. Gold and platinum increased until reaching peak values at 80 keV. The contrast of bismuth continued to increase up to 90 keV.

Separability

Separability between two materials was calculated using a previously-described technique⁵³ in terms of the separability index. This method calculates the expected overlap in signal component between two materials of interest. A technique or threshold choice that offers higher separability between two materials would offer a higher chance to distinguish those two materials minimizing confusion between the two.

The high energy image threshold value that generated the peak separability for each pair of materials is shown (Fig. 4). Separability of gadolinium and bismuth with iodine is of particular interest (Fig. 5a). The iodine/

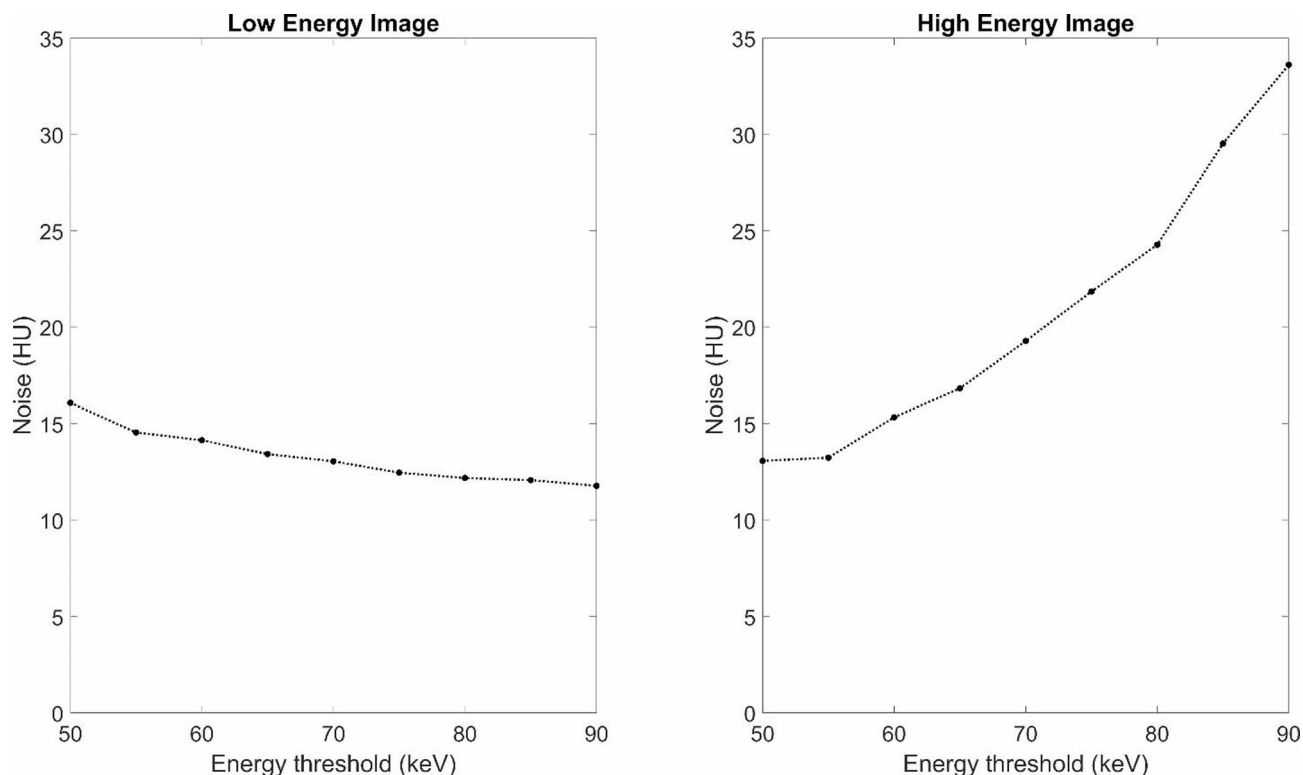


Fig. 2. Image noise (y-axis) as a function of energy threshold (x-axis). Noise was measured in a central water background region of interest.

gadolinium pair maintained a comparable level of separability across all thresholds. The separability of the iodine/bismuth pair steadily increased with energy threshold.

Separability between iodine and each of the nanomaterial agents increased until it reached a peak at the threshold closest to that material's k-edge and steadily decreased from that point (Fig. 5b). Tantalum had the highest separability at all thresholds except 80 keV where both platinum and gold had a comparable value.

When comparing their separability to one another (Fig. 6), the lanthanides that had k-edges close to one another had low separability. Higher thresholds caused the lowest separability for all combinations of lanthanides while peak separability was between 55 and 65 keV depending on the lanthanide pair.

Discussion

The primary goal of this study was to characterize signal and separability properties of materials in spectral CT in relation to the energy threshold. This was accomplished via simulation of a clinical photon-counting CT system to image a cylindrical water phantom containing materials of interest. We found that for specific materials, signal peaked with an energy threshold value just above that material's k-edge, and that for pairs of materials, the highest separability was maximized by the threshold that best separated the k-edges of those materials.

As the focus of this study was on change in signal characteristics due to the interaction of material properties and specific acquisition parameters, the simulated setup was chosen to minimize signal variations due to other external factors. By using a simple cylindrical phantom with a fixed size and water background, several complex effects were simplified in our signal calculations. First, the size of the phantom influences detected signal due to photon starvation. A larger phantom size requires a longer path-length for each individual photon which results in fewer photons reaching the detector and reduces the overall quality of signal^{54,55}. We would expect a direct relationship between phantom size and the reported signals and separabilities in this study. This effect would be particularly magnified for those materials with a lower k-edge as low energy photons are more susceptible to beam hardening. Second, a tissue background that more realistically reflected the complexity and heterogeneity of human patients would introduce further uncertainty. Accounting for different tissue types, structural noise variations, and textures would further obscure the targeted signal. Consideration of these more complex scenarios using size variant and anthropomorphic human phantoms will be considered in future studies.

From the image quality analysis, the most important finding was the relationship between noise and the upper energy threshold. As the threshold was increased fewer photons were used to form the high energy image causing noise in the higher energy image to rapidly increase. For materials, such as platinum, gold, and bismuth, where a higher value for the upper threshold maximized signal or separation from other materials, the impact of noise needs to be carefully monitored. This is particularly relevant for any post-processing applications, such as material decomposition, where noise in acquired images rapidly propagates in the post-processing workflow^{56,57}.

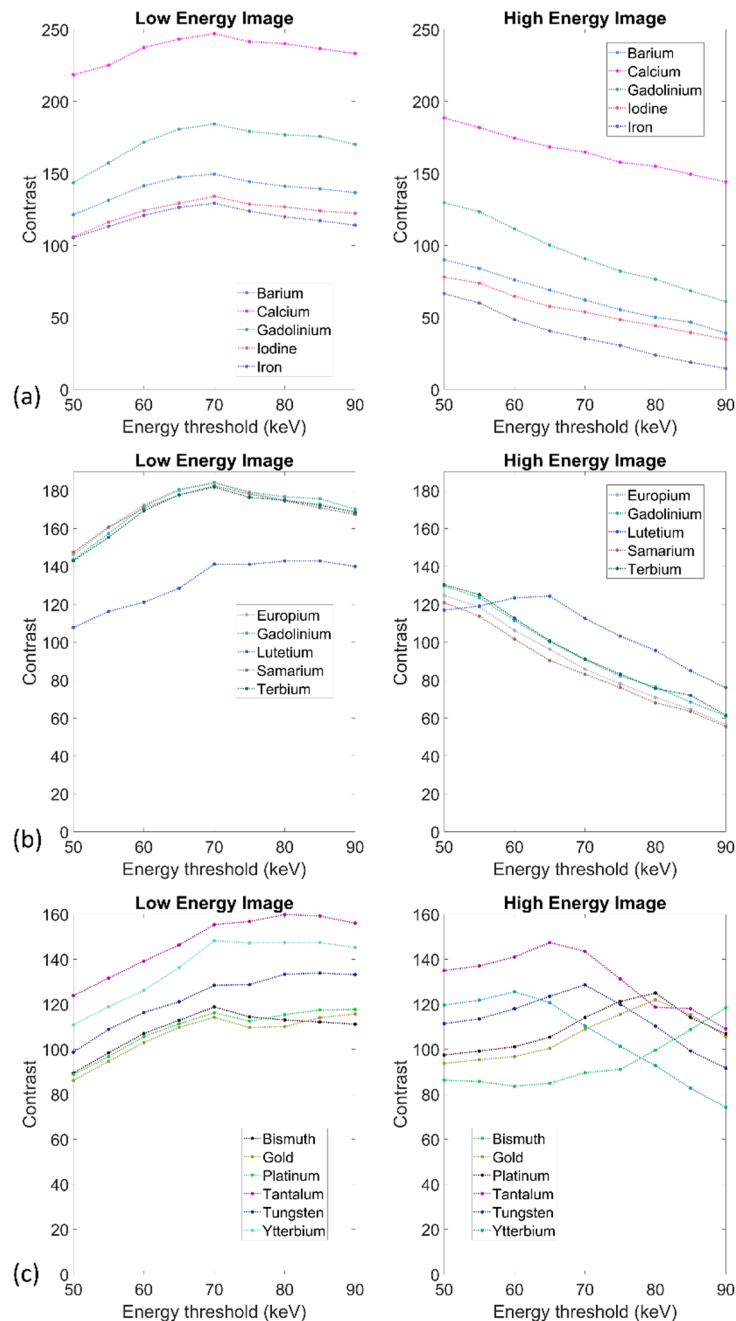


Fig. 3. (a) Contrast (y-axis) as a function of energy threshold (x-axis) for common biological materials and currently used contrast agents. Low energy image on the left and high energy image on the right. (b) Contrast (y-axis) as a function of energy threshold (x-axis) for lanthanides. Low energy image on the left and high energy image on the right. (c) Contrast (y-axis) as a function of energy threshold (x-axis) for candidate nanomaterials and contrast agents. Low energy image on the left and high energy image on the right.

Measures to mitigate the noise deficit can include hardware changes to increase overall signal, such as increasing tube voltage or current, and software corrections, including reconstruction parameters and noise correction.

Another relevant finding from the image quality analysis was the impact of the k-edge effect. Across all material groups, the signal characterization clearly demonstrated the k-edge effect based on the location of the signal peaks. For several materials, particularly in group two, the contrast peak occurred closer to 70 keV than a lower value as would be expected which may be attributed to the combination of the k-edge effect and the overall shape of the x-ray spectrum. The findings from this section of the study can help inform the selection of energy thresholds when considering single contrast material scenarios. Proper selection of energy thresholds can extract maximum signal while minimizing the impact of noise when a single contrast material is used.

Separability between materials is an important precondition for material decomposition as identification and quantification relies on distinguishable signals. In this work, this was characterized using the separability index.

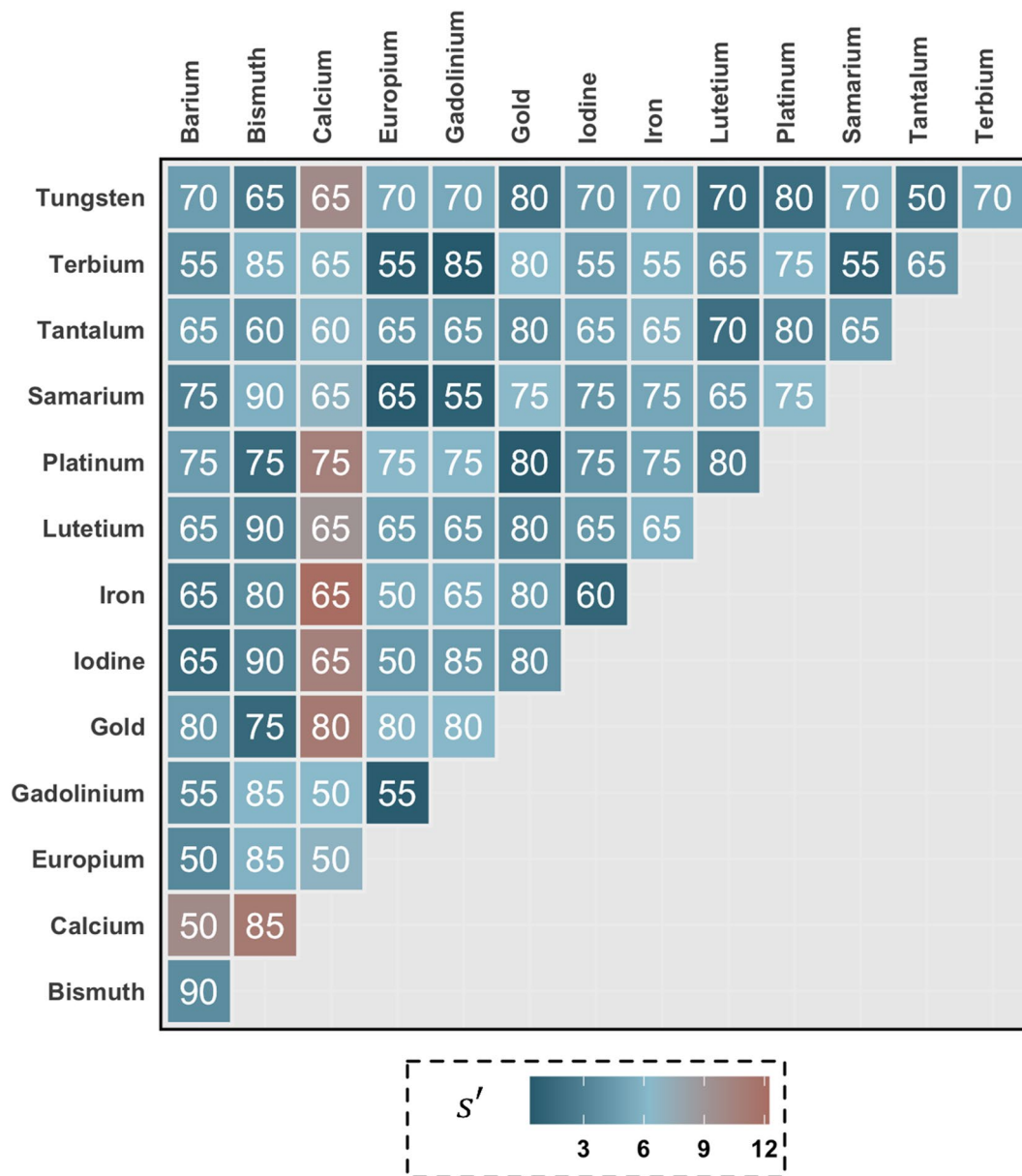


Fig. 4. High energy image threshold values (keV) that generate the highest separability for each pair of materials. Separability (s') between pairs of materials is illustrated by the color shading of each cell. The numbers within each cell indicate the high energy threshold value that provided the most separation between those two materials.

When comparing two sets of imaging parameters for a pair of materials, the parameters resulting in a higher separability index indicate that the materials in that pair are easier to differentiate than parameters with lower separability. The separability index accounts for the impact on signal overlap due to image formation factors including material concentration and reconstruction conditions. Notably, small differences in attenuation due to similar material concentrations are more difficult to separate than a scenario where a single material has much greater concentration than the other. As such, the material concentrations in this study were chosen to produce similar attenuation levels between pairs of materials to simulate more difficult separability scenarios. In general, in the presence of k-edge enhanced signals, such separation is more obvious with a threshold selection that emphasizes the difference between those signals. As shown in the separability comparison of lanthanide materials, pairs of materials that had a smaller k-edge difference were more difficult to separate, while the highest separability values were between lanthanide pairs that had a larger separation between their k-edge values. While determination of specific limits of separability for different clinical systems is a task for future studies, the results in this study can be used to inform which pairs of materials can be considered for multi-material contrast tasks.

The materials chosen in this study included agents that are used or are under investigation for clinical applications. Both gadolinium⁴⁴ and bismuth²⁹ have been investigated as dual contrast agents to be deployed

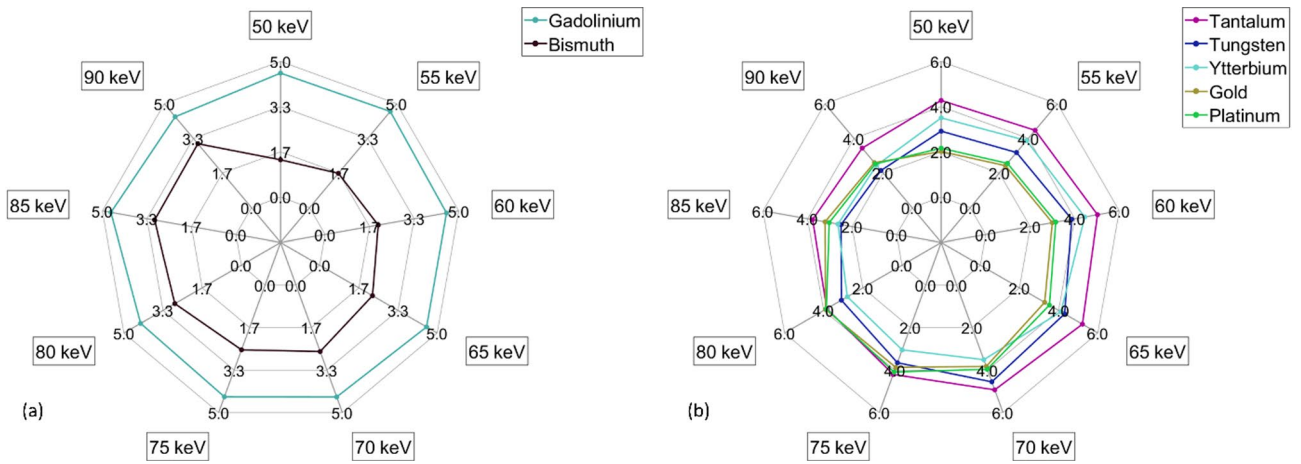


Fig. 5. Separability of iodine and potential dual contrast agents. (a) Spider plot showing the separability of gadolinium and bismuth with iodine. (b) Spider plot showing the separability of candidate nanomaterials with iodine.

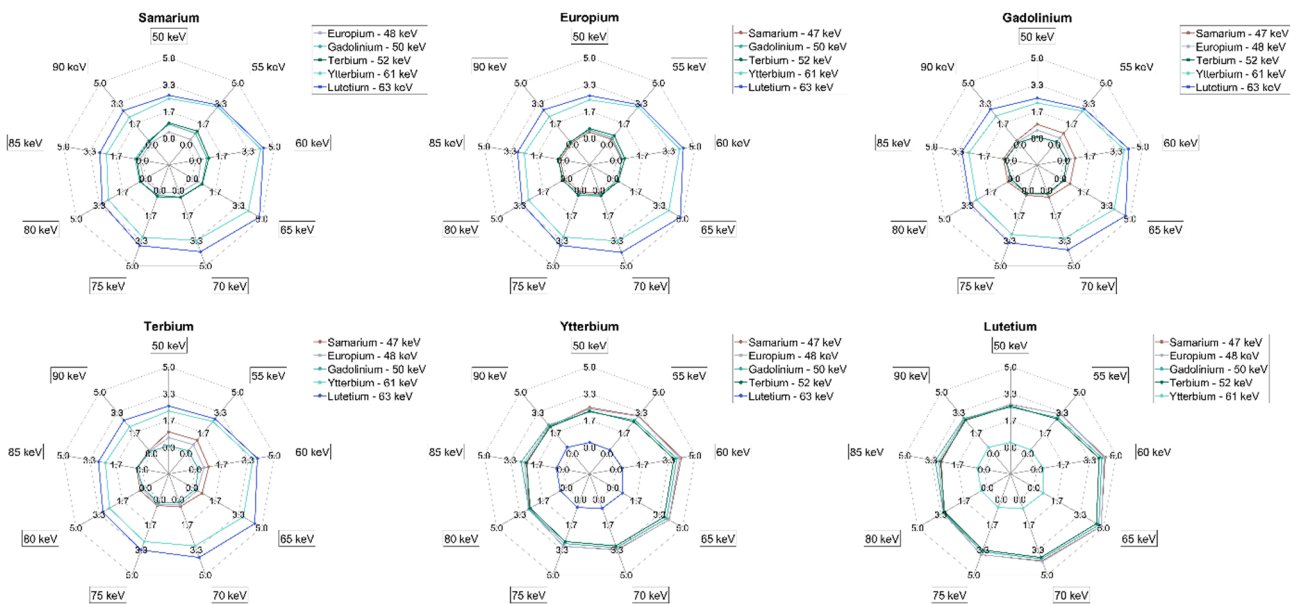


Fig. 6. Spider plots showing the separability of each lanthanide with the other lanthanide agents. Plots ordered by atomic number and k-edge: (a) Samarium, (b) Europium, (c) Gadolinium, (d) Terbium, (e) Ytterbium, (f) Lutetium.

along with iodine. Multi-contrast CT imaging offers two potential clinical benefits. First, contrast agents can be administered in different ways to directly image two areas as accomplished in studies by Ren et al.²⁹ who administered a bismuth solution in the gastrointestinal tract followed by intravenous iodine. Second, by delaying the time of injection between two contrast agents, it becomes possible to image multiple phases with a single acquisition. Symons et al.²⁴ administered gadolinium followed by iodine which allowed imaging of arterial and delayed renal enhancement and distinction of both from bismuth administered orally. In an occlusion-reperfusion model of myocardial infarction, Symons et al.²³ injected gadolinium followed later by iodine allowing imaging of early and late myocardial perfusion. Dual-phase imaging can reduce the overall radiation dose for multi-phase scanning by reducing the overall number of scans required. Nanomaterials offer a different opportunity to extend the application of clinical CT. As nanoparticles can be tagged to different molecules of interest³², they can be used for targeted imaging of different regions and functions thus enabling functional imaging with CT.

The lanthanides, outside of gadolinium and ytterbium, are not being widely considered for usage in clinical CT due to potential biocompatibility issues, including toxicity. There are potential uses of these materials for pre-clinical science such as simultaneous imaging of multiple agents or drug development with embolic beads.

However, the primary reason for their inclusion was their convenient k-edge range (47–63 keV) which falls in the range of the most commonly used energy thresholds in photon-counting CT. As a result, the lanthanides represent a set of materials that may be used to answer more fundamental questions regarding the separability of materials and the relationship between material k-edges and energy thresholds.

While the development of new contrast agents and nanomaterials offer exciting opportunities to expand the capabilities of diagnostic imaging, there are some considerations before eventual clinical adoption. Many current spectral CT systems, including the one modeled in this study, use two energy channels for their primary acquisition. Conventional approaches to material decomposition are limited to two or three material classes with such an acquisition. Future developments in hardware to include additional imaging channels and software with improved artificial intelligence guided material decomposition may address this challenge. This work represents an important characterization along this trajectory as *in silico* methods can help define design parameters for future systems and provide data for the development of new algorithms and applications. While we characterized a current clinical system, the statistical methodology used in this work can provide an approach for determining how to best image contrast agents with future systems.

There were some limitations to this study. First, the material concentrations used in this study were chosen to produce similar attenuation to the clinical standard for iodine. In practice, non-iodine materials may need different concentrations in the clinic to account for concerns of toxicity and signal strength. Second, only one spectral CT system was modeled. The sensitivity of separation between materials may vary due to the specifics of different spectral CT scanners as they become available for clinical use and how they achieve spectral separation. For other and future systems, particularly those with more energy bins than the system modeled in this study, an evaluation like our study would have to be performed. Third, the energy spectrum we used was at 120 kV. A higher kV of 140 will generate different but likely similar trends to those seen in this work. Finally, the current study modeled only two energy thresholds. Incorporation of additional energy levels would enable multi-material acquisitions beyond those in this study and is a topic for future evaluation.

Conclusion

With the development of spectral CT, material identification and quantification across different energy levels has become possible. This has led to an increased interest in materials and nanomaterials that can function as contrast agents, alone or with the clinical standard material of iodine where the two materials may be distinctly identified. In this study, we examined the signal properties and separability of those signals for several candidate materials with varying energy threshold. The impact of the k-edge energy levels on energy threshold selection was shown. Signal was maximized by the selection of a threshold that fell just above the k-edge of materials. For pairs of materials, the threshold value that separated the k-edge signals the best was shown to maximize separability, with specific quantitative results for specific material pairs.

Methods and materials

CT simulation pipeline

Simulations in this study were generated using the DukeSim (Duke University, USA) CT simulation platform⁴³. The simulator enables realistic simulation of CT acquisitions by incorporating scanner-specific geometry, physics and protocol conditions⁵⁸ and has been validated for both conventional and photon-counting CT systems⁵⁹. The photon-counting CT detector model was provided by the vendor and includes modeling of cross-talk and pulse pileup corrections.

The simulation pipeline requires information on the object to be imaged, the material properties of that object, and details of the imaging system to be modeled. Computational phantoms are used to represent the patient or object. Scanner properties include hardware information, such as detector and x-ray source conditions, as well as acquisition parameters, such as tube rotation speed and x-ray tube conditions. Two modules are used to carry out the simulation. First, a ray-tracing module is used to generate the primary signal at the detector. Second, a Monte Carlo module⁶⁰ is used to estimate scatter signal and dose. The outputs from both modules are post-processed for additional steps including tube current modulation⁵⁸, noise addition, and air/water corrections. The final outputs are generated as projection images. Images were reconstructed using the Multi-Channel Reconstruction⁶¹ toolkit.

Simulation design and image acquisition protocol

In this study, a clinical photon-counting CT system⁶² (NAEOTOM Alpha, Siemens Healthineers, Forchheim, Germany) was modeled operating in QPlus mode which uses two energy thresholds, a 144×0.4 mm collimation, and 0.4×0.4 mm in-plane pixels. Acquisitions were done with a fixed tube voltage (120 kV) and dose (tube current – 313 mAs, $CTDI_{vol}$ – 24.0 mGy). Images were simulated with a fixed low threshold at 20 keV while the higher energy threshold was varied between 50 and 90 keV in steps of 5 keV. The resulting output was two images for each acquisition condition: a low energy image containing signal from photons between the two thresholds and a high energy image containing signal between the high threshold and the maximum value of 120 kV. Images were reconstructed with filtered-back projection and 0.5×0.5 mm pixels. Images were denoised using 3-D Gaussian filtering (*imgaussfilt3* function, MATLAB, v2021a, MathWorks, Natick, MA) before further processing.

Image quality evaluation

In each image, circular regions of interest (ROI) were drawn in each vial and voxel values extracted for further analysis. An additional circular ROI was drawn in the water background. Image quality was evaluated as noise for each image and contrast between each material insert. Noise was characterized by the standard deviation

of voxel intensities within the water background ROI. Contrast between each material and background was calculated by

$$\text{Contrast} = \mu_{\text{insert}} - \mu_{\text{background}} \quad (1)$$

where μ_i represents the mean value within each ROI. Contrast was calculated separately for both low and high energy images.

Separability evaluation

To evaluate the separability between materials, a separability index⁵³ was used to compare each material at every energy threshold level. For two given regions of interest, this method calculates the expected overlap in signal component. The distribution of intensities within each multi-energy ROI is modeled as a multivariate random process with a deterministic signal and a stochastic noise component. Each variate represents a different energy level in the original spectral CT acquisition. The linear Hotelling observer⁶³ is used to calculate a test statistic λ for an ROI of interest. The test statistic represents the probability that a randomly chosen voxel value belongs to a particular material and the calculation of the test statistic accounts for factors that influence signal quality including material concentration. For two materials A and B, the separability index is defined as

$$s' = \frac{\bar{\lambda}_A - \bar{\lambda}_B}{\sqrt{\left(\frac{1}{2}\right) (\sigma_{\lambda_A}^2 + \sigma_{\lambda_B}^2)}} \quad (2)$$

where $\bar{\lambda}$ and σ_{λ}^2 represent the mean and variance for each test statistic.

Data availability

The data used to support the findings of this study are available from the corresponding author upon request.

Received: 2 May 2025; Accepted: 23 September 2025

Published online: 05 February 2026

References

- Fazel, R. et al. Exposure to low-dose ionizing radiation from medical imaging procedures. *N. Engl. J. Med.* **361**, 849–857 (2009).
- Mahesh, M., Ansari, A. J. & Mettler, F. A. Jr Patient exposure from radiologic and nuclear medicine procedures in the United States and worldwide: 2009–2018. *Radiology* **307**, e221263 (2022).
- Prince, J. L. & Links, J. M. *Medical Imaging Signals and Systems* Vol. 37 (Pearson Prentice Hall Upper Saddle River, 2006).
- Jackson, D. F. & Hawkes, D. J. X-ray Attenuation coefficients of elements and mixtures. *Phys. Rep.* **70**, 169–233 (1981).
- McCollough, C. H., Leng, S., Yu, L. & Fletcher, J. G. Dual-and multi-energy CT: principles, technical approaches, and clinical applications. *Radiology* **276**, 637–653 (2015).
- McCollough, C. H. et al. Principles and applications of multienergy CT: report of AAPM task group 291. *Med. Phys.* **47**, e881–e912 (2020).
- Johnson, T. R. Dual-energy CT: general principles. *Am. J. Roentgenol.* **199**, S3–S8 (2012).
- Greffier, J. et al. CT imaging: technical principles of dual-energy CT and multi-energy photon-counting CT. *Diagn. Interv. Imaging.* **104**, 167–177 (2023).
- Flohr, T. et al. Photon-counting CT review. *Physica Med.* **79**, 126–136 (2020).
- Flohr, T. & Schmidt, B. Technical basics and clinical benefits of photon-counting CT. *Invest. Radiol.* **58**, 441–450 (2023).
- Parakh, A. et al. Dual-Energy CT images: pearls and pitfalls. *RadioGraphics* **41**, 98–119 (2021).
- Ananthakrishnan, L. et al. Spectral detector CT-derived virtual non-contrast images: comparison of Attenuation values with unenhanced CT. *Abdom. Radiol.* **42**, 702–709 (2017).
- Sauter, A. P. et al. Dual-layer spectral computed tomography: virtual non-contrast in comparison to true non-contrast images. *Eur. J. Radiol.* **104**, 108–114 (2018).
- Yu, L. et al. Virtual monochromatic imaging in dual-source dual-energy CT: radiation dose and image quality. *Med. Phys.* **38**, 6371–6379 (2011).
- Albrecht, M. H. et al. Review of clinical applications for virtual monoenergetic dual-energy CT. *Radiology* **293**, 260–271 (2019).
- Landry, G. et al. Extracting atomic numbers and electron densities from a dual source dual energy CT scanner: experiments and a simulation model. *Radiother. Oncol.* **100**, 375–379 (2011).
- Saito, M. & Sagara, S. A simple formulation for deriving effective atomic numbers via electron density calibration from dual-energy CT data in the human body. *Med. Phys.* **44**, 2293–2303 (2017).
- Alvarez, R. E. & Macovski, A. Energy-selective reconstructions in x-ray computerised tomography. *Phys. Med. Biol.* **21**, 733 (1976).
- Long, Y. & Fessler, J. A. Multi-material decomposition using statistical image reconstruction for spectral CT. *IEEE Trans. Med. Imaging.* **33**, 1614–1626 (2014).
- Schlomka, J. et al. Experimental feasibility of multi-energy photon-counting K-edge imaging in pre-clinical computed tomography. *Phys. Med. Biol.* **53**, 4031 (2008).
- Roessl, E. & Proksa, R. K-edge imaging in x-ray computed tomography using multi-bin photon counting detectors. *Phys. Med. Biol.* **52**, 4679 (2007).
- Roessl, E. et al. Sensitivity of Photon-Counting based K-Edge imaging in X-ray computed tomography. *IEEE Trans. Med. Imaging.* **30**, 1678–1690 (2011).
- Symons, R. et al. Dual-contrast agent photon-counting computed tomography of the heart: initial experience. *Int. J. Cardiovasc. Imaging.* **33**, 1253–1261 (2017).
- Symons, R. et al. Photon-counting CT for simultaneous imaging of multiple contrast agents in the abdomen: an in vivo study. *Med. Phys.* **44**, 5120–5127 (2017).
- Ren, L., Rajendran, K., McCollough, C. H. & Yu, L. Radiation dose efficiency of multi-energy photon-counting-detector CT for dual-contrast imaging. *Phys. Med. Biol.* **64**, 245003 (2019).
- Yeh, B. M. et al. Opportunities for new CT contrast agents to maximize the diagnostic potential of emerging spectral CT technologies. *Adv. Drug Deliv. Rev.* **113**, 201–222 (2017).

27. van Hamersvelt, R. W. et al. Feasibility and accuracy of dual-layer spectral detector computed tomography for quantification of gadolinium: a Phantom study. *Eur. Radiol.* **27**, 3677–3686 (2017).
28. Bae, K. T. et al. Gadolinium-enhanced computed tomography angiography in multi-detector row computed tomography: initial observations. *Acad. Radiol.* **11**, 61–68 (2004).
29. Ren, L., Rajendran, K., Fletcher, J. G., McCollough, C. H. & Yu, L. Simultaneous Dual-Contrast imaging of small bowel with iodine and bismuth using Photon-Counting-Detector computed tomography: A feasibility animal study. *Invest. Radiol.* **55**, 688–694 (2020).
30. Shilo, M., Reuveni, T., Motiei, M. & Popovtzer, R. Nanoparticles as computed tomography contrast agents: current status and future perspectives. *Nanomedicine* **7**, 257–269 (2012).
31. Cormode, D. P., Naha, P. C. & Fayad, Z. A. Nanoparticle contrast agents for computed tomography: a focus on micelles. *Contrast Media Mol. Imaging.* **9**, 37–52 (2014).
32. Aslan, N., Ceylan, B., Koç, M. M. & Findik, F. Metallic nanoparticles as X-Ray computed tomography (CT) contrast agents: A review. *J. Mol. Struct.* **1219**, 128599 (2020).
33. Ashrafi, K. et al. Characterization of a novel intrinsically radiopaque drug-eluting bead for image-guided therapy: DC bead LUMI™. *J. Controlled Release.* **250**, 36–47 (2017).
34. Negussie, A. H. et al. Synthesis, characterization, and imaging of radiopaque bismuth beads for image-guided transarterial embolization. *Scientific Reports* **11**, 533 (2021).
35. Cormode, D. P. et al. Multicolor spectral photon-counting computed tomography: in vivo dual contrast imaging with a high count rate scanner. *Sci. Rep.* **7**, 4784 (2017).
36. Pan, D. et al. Molecular imaging with spectral CT nanoprobe in Design and Applications of Nanoparticles in Biomedical Imaging (eds Bulte, J. W. M. & Modo M. M. J.) 385–402 (Springer, 2017).
37. Fornaro, J. et al. Dual-and multi-energy CT: approach to functional imaging. *Insights into Imaging.* **2**, 149–159 (2011).
38. FitzGerald, P. F. et al. CT image contrast of high-Z elements: Phantom imaging studies and clinical implications. *Radiology* **278**, 723–733 (2016).
39. Kim, J. et al. Assessment of candidate elements for development of spectral photon-counting CT specific contrast agents. *Sci. Rep.* **8**, 12119 (2018).
40. Abadi, E. et al. Virtual clinical trials in medical imaging: a review. *J. Med. Imaging.* **7**, 042805 (2020).
41. Samei, E. et al. In *Medical Imaging 2020: Physics of Medical Imaging, Vol. 11312 113121T* (International Society for Optics and Photonics, 2020).
42. Abadi, E. et al. Toward widespread use of virtual trials in medical imaging innovation and regulatory science. *Medical Physics* **51** (2024).
43. Abadi, E. et al. DukeSim: a realistic, rapid, and scanner-specific simulation framework in computed tomography. *IEEE Trans. Med. Imaging.* **38**, 1457–1465 (2018).
44. Ren, L. et al. Dual-contrast biphasic liver imaging with iodine and gadolinium using photon-counting detector computed tomography: an exploratory animal study. *Invest. Radiol.* **57**, 122 (2022).
45. Liu, Y. et al. A high-performance ytterbium-based nanoparticulate contrast agent for in vivo X-ray computed tomography imaging. *Angew. Chem.* **124**, 1466–1471 (2012).
46. Dong, Y. C. et al. Ytterbium nanoparticle contrast agents for conventional and spectral Photon-Counting CT and their applications for hydrogel imaging. *ACS Appl. Mater. Interfaces.* **14**, 39274–39284 (2022).
47. Lambert, J. W. et al. An intravascular tantalum oxide-based CT contrast agent: preclinical evaluation emulating overweight and obese patient size. *Radiology* **289**, 103–110 (2018).
48. Koshevaya, E., Krivoschapina, E. & Krivoschapkin, P. Tantalum oxide nanoparticles as an advanced platform for cancer diagnostics: a review and perspective. *J. Mater. Chem. B.* **9**, 5008–5024 (2021).
49. Kim, S. J. et al. Synthesis of nanoparticle CT contrast agents: in vitro and in vivo studies. *Science Technol. Adv. Materials* **16** (2015).
50. Aziz, F. et al. Novel route synthesis of porous and solid gold nanoparticles for investigating their comparative performance as contrast agent in computed tomography scan and effect on liver and kidney function. *Int. J. Nanomed.* **12**, 1555 (2017).
51. Keshavarz, M. et al. Alginate hydrogel co-loaded with cisplatin and gold nanoparticles for computed tomography image-guided chemotherapy. *J. Biomater. Appl.* **33**, 161–169 (2018).
52. Jeyaraj, M., Gurunathan, S., Qasim, M., Kang, M. H. & Kim J.-H. A comprehensive review on the synthesis, characterization, and biomedical application of platinum nanoparticles. *Nanomaterials* **9**, 1719 (2019).
53. Rajagopal, J. R. et al. Development of a separability index for task specific characterization of spectral computed tomography. *Physica Med.* **122**, 103382 (2024).
54. Pelgrim, G. J. et al. Accuracy of iodine quantification using dual energy CT in latest generation dual source and dual layer CT. *Eur. Radiol.* **27**, 3904–3912 (2017).
55. Lambert, J. W. et al. The effect of patient diameter on the dual-energy ratio of selected contrast-producing elements. *J. Comput. Assist. Tomogr.* **41**, 505 (2017).
56. Primak, A., Ramirez Giraldo, J., Liu, X., Yu, L. & McCollough, C. H. Improved dual-energy material discrimination for dual-source CT by means of additional spectral filtration. *Med. Phys.* **36**, 1359–1369 (2009).
57. Ren, L., McCollough, C. H. & Yu, L. in *Medical Imaging 2018: Physics of Medical Imaging*, Vol. 10573 363–368SPIE, (2018).
58. Jadick, G. et al. A scanner-specific framework for simulating CT images with tube current modulation. *Phys. Med. Biol.* **66**, 185010 (2021).
59. Abadi, E. et al. Development of a scanner-specific simulation framework for photon-counting computed tomography. *Biomedical Phys. Eng. Express.* **5**, 055008 (2019).
60. Sharma, S., Abadi, E., Kapadia, A., Segars, W. P. & Samei, E. A GPU-accelerated framework for rapid Estimation of scanner-specific scatter in CT for virtual imaging trials. *Phys. Med. Biol.* **66**, 075004 (2021).
61. Clark, D. P. & Badea, C. T. in *The Fifth International Conference on Image Formation in X-Ray Computed Tomography* Salt Lake City Utah, (2018).
62. Rajendran, K. et al. First clinical photon-counting-detector CT system: technical evaluation. *Radiology* **303**, 130 (2022).
63. Barrett, H. H., Yao, J., Rolland, J. P. & Myers, K. J. Model observers for assessment of image quality. *Proceedings of the National Academy of Sciences* **90**, 9758–9765 (1993).

Acknowledgements

This study was supported in part by the National Institutes of Health (NIH) Clinical Center Radiology and Imaging Sciences (RADIS), the NIH Graduate Partnership Program, the NIH Intramural Research Program and NIH grant P41EB028744. Author PS is an employee of Siemens Healthineers. Author ES lists relationships with the following entities unrelated to the present publication: GE, Siemens, Imaloxix, Metis Health Analytics, Cambridge University Press, and Wiley and Sons. The other authors list no competing interests. The contributions of the NIH authors were made as part of their official duties as NIH federal employees, are in compliance with agency policy requirements, and are considered Works of the United States Government. However, the findings and conclusions presented in this paper are those of the author(s) and do not necessarily reflect the views of the NIH or the U.S. Department of Health and Human Services.

Author contributions

Author JR and WP designed the research and wrote the manuscript. Author FF assisted with data analysis and helped prepare figure 3. Author PS provided expertise on spectral CT and material decomposition. Authors EJ provided clinical expertise. Author ES provided simulation tools and materials. All authors reviewed the manuscript.

Declarations

Competing interests

Author PS is an employee of Siemens Healthineers. Author ES lists relationships with the following entities unrelated to the present publication: GE, Siemens, Imalogix, Metis Health Analytics, Cambridge University Press, and Wiley and Sons. All the remaining authors declare no conflict of interest.

Additional information

Correspondence and requests for materials should be addressed to E.C.J.

Reprints and permissions information is available at www.nature.com/reprints.

Publisher's note Springer Nature remains neutral with regard to jurisdictional claims in published maps and institutional affiliations.

Open Access This article is licensed under a Creative Commons Attribution 4.0 International License, which permits use, sharing, adaptation, distribution and reproduction in any medium or format, as long as you give appropriate credit to the original author(s) and the source, provide a link to the Creative Commons licence, and indicate if changes were made. The images or other third party material in this article are included in the article's Creative Commons licence, unless indicated otherwise in a credit line to the material. If material is not included in the article's Creative Commons licence and your intended use is not permitted by statutory regulation or exceeds the permitted use, you will need to obtain permission directly from the copyright holder. To view a copy of this licence, visit <http://creativecommons.org/licenses/by/4.0/>.

This is a U.S. Government work and not under copyright protection in the US; foreign copyright protection may apply 2026